nature COMMUNICATIONS

ARTICLE

https://doi.org/10.1038/s41467-022-28480-9 OPEN

High-mobility hydrogenated polycrystalline In_2O_3 (In_2O_3:H) thin-film transistors

Yusaku Magari [1✉], Taiki Kataoka[2], Wenchang Yeh[1] & Mamoru Furuta[2,3]

Oxide semiconductors have been extensively studied as active channel layers of thin-film transistors (TFTs) for electronic applications. However, the field-effect mobility (μ_{FE}) of oxide TFTs is not sufficiently high to compete with that of low-temperature-processed polycrystalline-Si TFTs (50–100 $cm^2V^{-1}s^{-1}$). Here, we propose a simple process to obtain high-performance TFTs, namely hydrogenated polycrystalline In_2O_3 (In_2O_3:H) TFTs grown via the low-temperature solid-phase crystallization (SPC) process. In_2O_3:H TFTs fabricated at 300 °C exhibit superior switching properties with $\mu_{FE} = 139.2\ cm^2V^{-1}s^{-1}$, a subthreshold swing of 0.19 $Vdec^{-1}$, and a threshold voltage of 0.2 V. The hydrogen introduced during sputter deposition plays an important role in enlarging the grain size and decreasing the subgap defects in SPC-prepared In_2O_3:H. The proposed method does not require any additional expensive equipment and/or change in the conventional oxide TFT fabrication process. We believe these SPC-grown In_2O_3:H TFTs have a great potential for use in future transparent or flexible electronics applications.

[1] Graduate School of Natural Science and Technology, Shimane University, Matsue, Shimane 690-8504, Japan. [2] School of Environmental Science and Engineering, Kochi University of Technology, Kami, Kochi 782-8502, Japan. [3] Center for Nanotechnology, Research Institute, Kochi University of Technology, Kami, Kochi 782-8502, Japan. ✉email: magari.yusaku@riko.shimane-u.ac.jp

Wide-bandgap oxide semiconductors (OSs) have been extensively studied as active channel layers of thin-film transistors (TFTs) for next-generation flat-panel displays[1,2], nonvolatile memories[3], inverters[4], various sensors[5,6], Schottky devices[7,8], and so on. Among OSs, amorphous In–Ga–Zn–O (a-IGZO) TFTs have now become the backplane standard for active-matrix liquid-crystal displays (AMLCDs) and active-matrix organic light-emitting diode (AMOLED) displays because of their reasonable field-effect mobility (μ_{FE}) of over 10 $cm^2 V^{-1} s^{-1}$, extremely low leakage current, low process temperature (<350 °C), and large-area scalability[9,10]. Although the μ_{FE} value of a-IGZO TFTs is more than ten times higher than that of hydrogenated amorphous Si (a-Si:H) TFTs (<1 $cm^2 V^{-1} s^{-1}$), it is not sufficiently high to compete with that of low-temperature-processed polycrystalline-Si (LTPS) TFTs (50–100 $cm^2 V^{-1} s^{-1}$)[11]. The main disadvantages of LTPS TFTs are a relatively high process temperature (450–550 °C) and an expensive crystallization process. The high μ_{FE} values of OS TFTs mean these devices could be used in fields that have been dominated by LTPS TFTs and in transparent and flexible devices that are incompatible with Si. Numerous types of approaches to enhance the μ_{FE} value of OS TFTs have been investigated, including cation composition[12,13], multiple channel structures[14,15], dual-gate architecture[16,17], metal capping layer structures[18,19], post treatment[20,21], and their combination. Among these, cation composition control is the most promising method. It requires no extra complex process for integrating OS TFTs. In-rich OSs have been studied extensively. The large spatial spread of the In 5*s* orbital with a large overlap can provide a facile electron transport path with a low electron effective mass[22]. However, undoped In_2O_3 films exhibit a high background electron concentration (10^{19}–10^{21} cm^{-3})[23,24], which is attributable to the presence of native defects, such as oxygen vacancies, making it difficult to control the threshold voltage of the TFTs[25,26]. To suppress the carrier concentration in In_2O_3, elements such as Ga, Hf, Si, Al, and W were added, which have large bond dissociation energies with oxygen[12]. Many AOS TFTs have been explored with multicomponent oxide semiconductors, such as In–W–Zn–O[27], Al–In–Sn–Zn–O[28], and In–Ga–Zn–Sn–O[29]. However, multicomponent oxides complicate the composition control of the deposited film. Moreover, multimetal cations cause potential fluctuation near the conduction band minimum, which might hinder electron transport[30].

Recently, crystalline OSs have been proposed to enhance the carrier mobility because the disorder-induced subgap states can be suppressed via lattice ordering. Yang et al. reported a μ_{FE} value of 60.7 $cm^2 V^{-1} s^{-1}$ for a TFT obtained using polycrystalline In–Ga–O annealed at 700 °C[31]. Although high annealing temperatures result in better electrical properties of the oxide active channel layer, such high temperatures are unsuitable for device application on glass or plastic substrates. Our group reported a μ_{FE} value of 50.6 $cm^2 V^{-1} s^{-1}$ for a TFT obtained using hydrogenated polycrystalline In–Ga–O formed via solid-phase crystallization (SPC) at 300 °C[32].

This study proposes a simple material and a simple process to obtain high-performance TFTs, namely hydrogenated polycrystalline In_2O_3 (In_2O_3:H) TFTs grown via the low-temperature SPC process. In_2O_3:H TFTs fabricated at 300 °C exhibit superior switching properties with $\mu_{FE} = 139.2$ $cm^2 V^{-1} s^{-1}$, a subthreshold swing (*SS*) of 0.19 V dec^{-1}, and a threshold voltage (V_{th}) of 0.2 V. The hydrogen introduced during sputter deposition plays an important role in enlarging the grain size and decreasing the subgap defects in SPC-prepared In_2O_3:H. The proposed method has great potential for future transparent or flexible electronics applications.

Results

Structural properties of the In_2O_3 and In_2O_3:H films. Figures 1a, b show the XRD patterns of the 50-nm-thick In_2O_3 and In_2O_3:H films deposited at various $R[H_2]$ values and at a constant $R[O_2]$ of 1%. For the as-deposited films (Fig. 1a), the In_2O_3 film without H_2 introduction exhibited a clear crystalline nature with the (222) preferred orientation of the cubic bixbyite In_2O_3 crystal. There was no noticeable peak for the In_2O_3:H films deposited at $R[H_2]$ values of 3 and 5%. This result indicates that H_2 addition suppresses the growth of crystallites during deposition. After annealing at 250 °C in nitrogen for 1 h, the amorphous phase of In_2O_3:H changed to the crystalline one with the (222) preferred orientation. The angles of the diffracted peaks are in good agreement with the In_2O_3 powder data (ICSD code: 14388). Moreover, the crystallized films exhibited smaller full-width at half-maximum values of the (222) reflection than the film deposited without hydrogen introduction, indicating larger crystallite sizes and smaller strains in the In_2O_3:H films.

Figure 1c–h depict the EBSD images along the normal direction for the In_2O_3 and In_2O_3:H films with and without annealing at 250 °C in nitrogen. For the as-deposited films (Fig. 1c–e), a randomly oriented small grain structure embedded in the amorphous matrix can be observed in the In_2O_3 film without H_2 introduction. The grain structure disappeared upon increasing the $R[H_2]$ value to 5%. In contrast, a huge grain structure appeared for In_2O_3:H deposited at $R[H_2] = 5\%$ after annealing at 250 °C (Fig. 1h), indicating SPC occurrence. This is consistent with the results of the XRD analysis shown in Fig. 1a, b. The corresponding area fractions of each lateral grain size are shown in Fig. 1i, j. The detected minimum grain size is around 15 nm, which is limited by the electron beam size of the EBSD measurements. For the as-deposited films (Fig. 1i), all films showed the maximum area fraction for a grain size of 15 nm; however, a small proportion of the area fraction with a grain size of ~70 nm was detected in the In_2O_3 film, indicating nuclei in the as-deposited film. After annealing at 250 °C (Fig. 1j), the peak of the area fraction shifted toward a larger grain size as $R[H_2]$ increased, and the In_2O_3:H film deposited at $R[H_2] = 5\%$ showed a maximum area fraction of 23% at a grain size of 140 nm. Furthermore, as $R[H_2]$ increased from 0 to 5%, the area fraction of the minimum grain size below 15 nm significantly decreased, and only a few small grains were in between the large grains, as shown in Fig. 1h. Similar results were observed for films annealed at 250 °C in ambient air (shown in Supplementary Fig. 1). The EBSD results show that the nuclei density in the as-deposited film was suppressed by introducing hydrogen during sputtering. Because of the reduction in the nuclei density in the initial In_2O_3:H film, the grain size of the In_2O_3:H film could be enlarged through SPC. Thus, the XRD and EBSD results indicate that controlling the crystallinity and nuclei density in the as-deposited film are key factors to achieve high-quality In_2O_3:H films.

Electrical and optical properties of the In_2O_3 and In_2O_3:H films. Figure 2a–d show the carrier concentration (N_e) and Hall mobility (μ_H) of the 50-nm-thick In_2O_3 and In_2O_3:H films deposited at various $R[H_2]$ values as a function of the annealing temperature (T_{ann}). Koida et al. reported that both the N_e and μ_H of the SPC-prepared In_2O_3:H films decrease dramatically for the films annealed in vacuum at $T_{ann} > 400$ °C due to the desorption of the H_2O and H_2 gases from the films and additional microscopic defects inside the grains[33]. The electrical properties of OSs are strongly affected by the annealing atmosphere[34]; thus, annealing treatments at temperatures ranging from 150 to 350 °C in nitrogen and ambient air were examined. For the as-deposited films, N_e increased from 7.1×10^{19} to 5.7×10^{20} cm^{-3} upon increasing $R[H_2]$ from 0 to 5%, as shown in Fig. 2a. Since

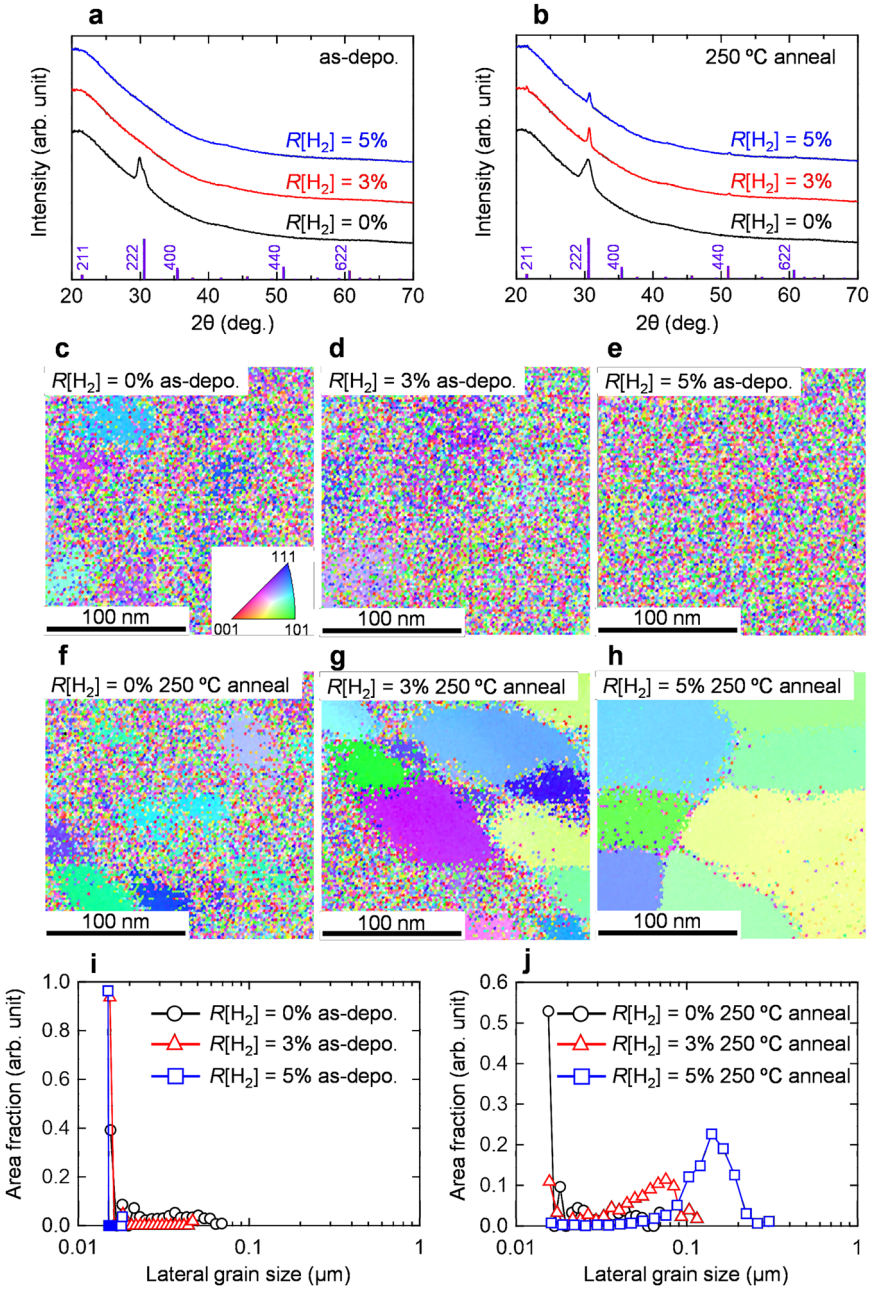

Fig. 1 Structural properties of the In_2O_3 and In_2O_3:H films. XRD patterns of the In_2O_3 and In_2O_3:H films deposited at different $R[H_2]$ values and at a constant $R[O_2]$ value of 1% **a** before and **b** after annealing at 250 °C in N_2. EBSD images of the In_2O_3 and In_2O_3:H films deposited at different $R[H_2]$ values **c**–**e** before and **f**–**h** after annealing at 250 °C in N_2. Area fraction of each grain size obtained from the In_2O_3 and In_2O_3:H films deposited at different $R[H_2]$ values **i** before and **j** after annealing at 250 °C in N_2.

hydrogen acts as a shallow donor in In_2O_3[35], the increase in the N_e of the as-deposited In_2O_3:H film upon increasing $R[H_2]$ is attributable to hydrogen doping effects. The In_2O_3 film deposited without hydrogen introduction exhibited an almost constant N_e value over the whole range of investigated T_{ann} values irrespective of the annealing atmosphere, as shown in Fig. 2a, c. In contrast, there was a strong dependence of N_e on the annealing atmosphere for the In_2O_3:H films. The N_e of the In_2O_3:H film annealed in N_2 gradually decreased with increasing T_{ann} (Fig. 2a), whereas the N_e of the In_2O_3:H film annealed in air rapidly decreased for $T_{ann} >$ 200 °C (Fig. 2c). In addition, the N_e reduction was remarkable in the In_2O_3:H film deposited at a higher $R[H_2]$ value. As a result, an appropriate N_e value of 2.0×10^{17} cm^{-3} for TFT fabrication was obtained at $T_{ann} = 300$ °C for the In_2O_3:H film deposited at $R[H_2] = 5\%$; this N_e value is over two orders of magnitude lower than that of the In_2O_3 film deposited without hydrogen introduction (3.0×10^{19} cm^{-3}). Such a large decrease in the N_e value of the In_2O_3:H films has not been reported before. Although adding H_2 induced the formation of free carriers in the as-deposited films, the N_e of the films could be reduced via the relatively low-temperature SPC process and became comparable to that of single-crystalline epitaxial In_2O_3 films deposited at 650 °C (~1×10^{17} cm^{-3})[36].

Regarding the Hall mobility of the films, In_2O_3 without hydrogen introduction exhibited an almost constant μ_H value over the entire range of investigated T_{ann} values irrespective of the annealing atmosphere, as shown in Fig. 2b, c. Upon annealing in N_2 at $T_{ann} = 200$ °C, the μ_H of In_2O_3:H increased to 78.6 $cm^2 V^{-1} s^{-1}$ at

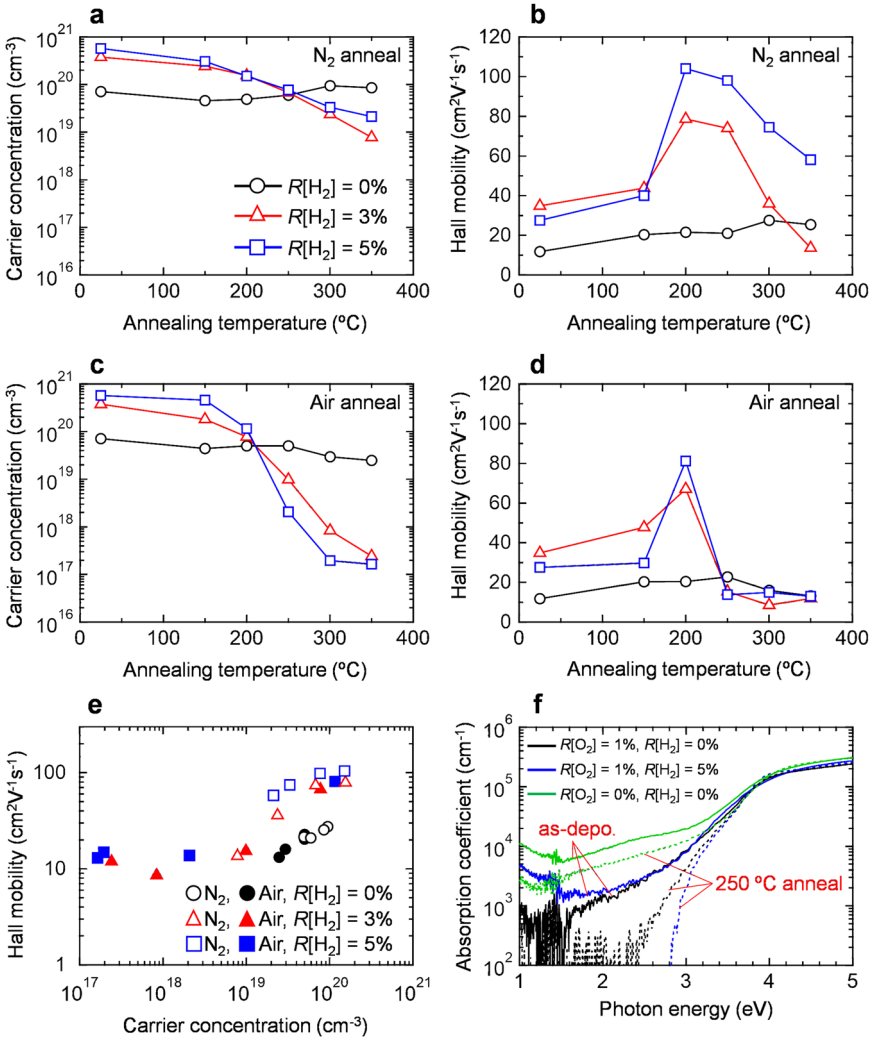

Fig. 2 Electrical and optical properties of the In_2O_3 and In_2O_3:H films. a N_e and **b** μ_H of In_2O_3 and In_2O_3:H deposited at different $R[H_2]$ values as a function of the annealing temperature in N_2. **c** N_e and **d** μ_H of In_2O_3 and In_2O_3:H deposited at different $R[H_2]$ values as a function of the annealing temperature in ambient air. **e** The relationship between μ_H and N_e for the films annealed at $T_{ann} > 200$ °C in N_2 and ambient air. **f** Optical absorption spectra of the 50-nm-thick In_2O_3 and In_2O_3:H films deposited at different $R[H_2]$ values before and after annealing at 250 °C in ambient air. In_2O_3 films deposited without oxygen and hydrogen are also shown for comparison.

$R[H_2] = 3\%$ and 104.0 $cm^2 V^{-1} s^{-1}$ at $R[H_2] = 5\%$, indicating that the SPC started at a T_{ann} value between 150 and 200 °C. Furthermore, the increased μ_H is attributable to the increased grain size, as shown in Fig. 1f–h. As T_{ann} increased, the μ_H of In_2O_3:H gradually decreased (Fig. 2b). Upon annealing in air (Fig. 2d), the maximum μ_H of In_2O_3:H decreased slightly to 67.1 $cm^2 V^{-1} s^{-1}$ at $R[H_2] = 3\%$ and 81.2 $cm^2 V^{-1} s^{-1}$ at $R[H_2] = 5\%$, and the decrease in μ_H for $T_{ann} > 250$ °C was confirmed.

To understand the transport properties of the In_2O_3:H films after SPC, the relationship between μ_H and N_e for the films annealed in the range of temperatures between 200 °C and 350 °C in N_2 and ambient air was summarized, as shown in Fig. 2e. The N_e of the In_2O_3:H film could be controlled by up to three orders of magnitude. Moreover, for the N_e range between 10^{19} and 10^{20} cm^{-3}, μ_H increases with increasing $R[H_2]$, which is attributable to the suppression of grain boundary scattering due to the increasing grain size. For all the films, μ_H increased with increasing N_e. In general, the grain boundaries have a small impact on μ_H in transparent conductive oxides with high N_e (>10^{20} cm^{-3}) because electrons can tunnel through the narrow width (<1 nm) of the grain barriers at high N_e values (>10^{20} cm^{-3}). However, grain boundary scattering is a dominant factor that limits the μ_H in films with lower N_e[37]. Thus, the observed decrease in μ_H with decreasing N_e (Fig. 2e) is due to grain boundary scattering. Although the μ_H of In_2O_3:H decreased for $N_e < 10^{19}$ cm^{-3}, carriers (with number in the range of 10^{19}–10^{20} cm^{-3}) will be generated at the In_2O_3:H/gate insulator interface of the TFTs when applying a voltage to the gate[15]; thus, a high μ_{FE} can be expected in In_2O_3:H TFTs.

Figure 2f shows the optical absorption (α) spectra of the In_2O_3 and In_2O_3:H films before and after annealing at 250 °C in ambient air. The green line represents the In_2O_3 film deposited without oxygen and hydrogen (only Ar gas), which is shown for comparison. The spectral features that arise as the photon energy exceeds 2.9 eV are due to the absorption associated with the interband transition in In_2O_3, whereas the features that arise when the photon energy is below 1.5 eV are due to free carrier absorption. The absorption in the subgap region (<2.9 eV) dropped as $R[O_2]$ increased from 0 to 1%, suggesting that oxygen deficiencies, which give rise to subgap defects, are compensated when sputtering in an oxidizing atmosphere. When hydrogen is added during sputter deposition, the absorption is enhanced in the subgap region for the as-deposited films, especially in the

photon energy region below 1.5 eV, indicating that free electron absorption is increased due to the hydrogen doping effect. On the other hand, after annealing at 250 °C in ambient air (dashed line), the absorption across the subgap of the In_2O_3:H film decreased significantly and was lower than that of the In_2O_3 film. Since subgap defects are generated from native defects, such as oxygen vacancies, as described above, it can be inferred that oxygen vacancies were efficiently reduced in In_2O_3:H via SPC in ambient air. This result is consistent with the Hall effect measurements, where it was found that N_e decreased from 5.7×10^{20} to 2.0×10^{18} cm^{-3} upon annealing in air at 250 °C, as shown in Fig. 2c. The structural, electrical, and optical properties of the In_2O_3:H films show that the hydrogen introduced during sputter deposition plays an important role in enlarging the grain size and decreasing the subgap defects after SPC, increasing μ_H and decreasing N_e. However, a more detailed study will be necessary to carry out quantitative evaluations of the carrier generation and scattering in the SPC-prepared In_2O_3:H films.

In_2O_3:H TFT characteristics. Figure 3a shows the picture and schematic cross-sectional view of the fabricated In_2O_3:H TFT. All TFTs were fabricated using annealing in ambient air at 300 °C. Figure 3c–e show typical transfer characteristics of the TFTs with In_2O_3 and In_2O_3:H channels deposited at various $R[H_2]$ values. The variations of μ_{FE}, subthreshold swing (SS), threshold voltage (V_{th}), and hysteresis (ΔV) were evaluated from ten TFTs on the same substrate. The μ_{FE} was calculated from the linear transfer characteristics as $\mu_{FE} = Lg_m/(WC_{ox}V_{ds})$ at $V_{ds} = 0.1$ V, where g_m is the transconductance, C_{ox} is the oxide capacitance of the gate insulator, and V_{ds} is the drain voltage. V_{th} was defined by gate voltage (V_{gs}) at drain current (I_{ds}) of 1 nA, and SS was extracted from V_{gs}, which required an increase in the I_{ds} from 10 to 100 pA. The In_2O_3 TFT without H_2 introduction (Fig. 3c) did not exhibit any switching (conductive behavior). By contrast, the In_2O_3:H TFT deposited at $R[H_2] = 5\%$ exhibited a switching with an extremely high μ_{FE} of 139.2 $cm^2 V^{-1} s^{-1}$, a SS of 0.19 V dec^{-1}, a V_{th} of 0.2 V, and a ΔV of 0.3 V as shown in Table 1. The TFT with In_2O_3:H deposited at $R[H_2] = 5\%$ showed a slightly small SS value (0.19 V dec^{-1}) compared with that of the TFT with In_2O_3:H deposited at $R[H_2] = 3\%$ (0.41 V dec^{-1}). The subgap density of states (D_{sg}) at the Fermi level was calculated as $SS = dV_{gs}/d\log I_{ds} = \ln 10\ k_BT/e\ (1 + eD_{sg}/C_{ox})$, where k_B is Boltzmann's constant and e is the elementary electric charge[10]. The D_{sg} decreased from 1.3×10^{12} to 4.7×10^{11} $cm^{-2} eV^{-1}$ by increasing the $R[H_2]$ value from 3 to 5%. This result suggests that the disorder-originated subgap defect states near the conduction band minimum can be reduced in the In_2O_3:H channel deposited at

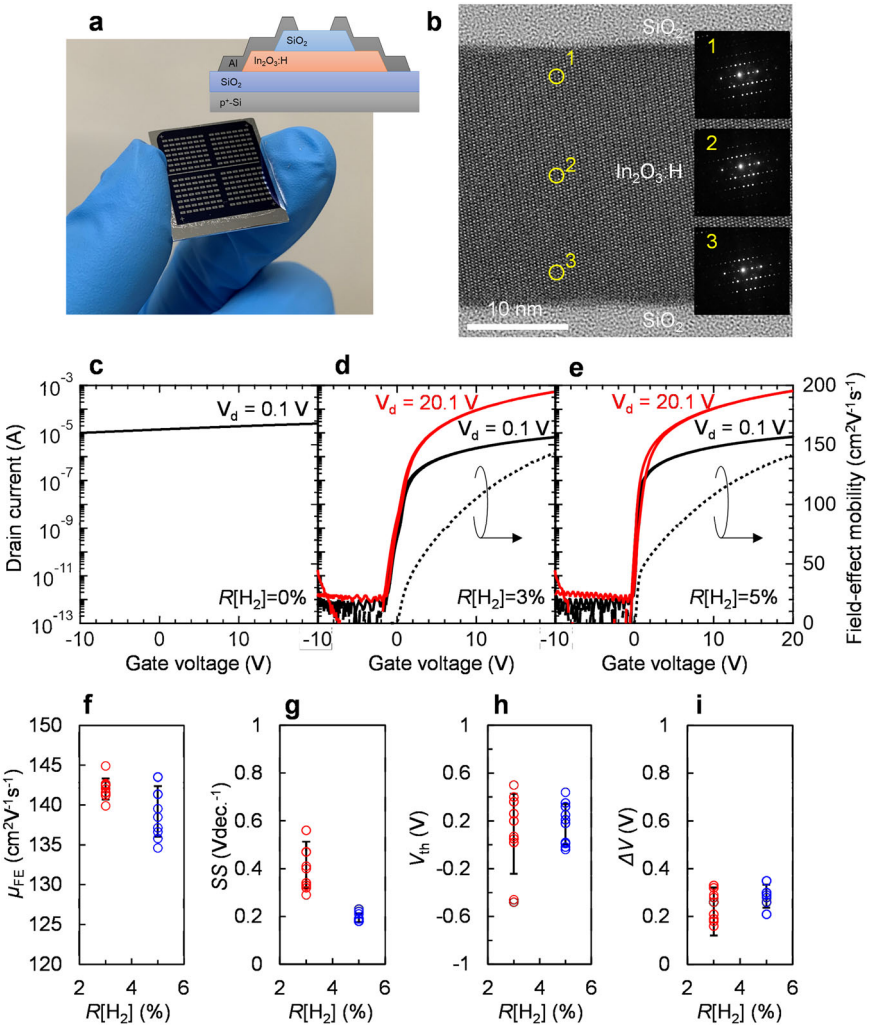

Fig. 3 In_2O_3:H TFT characteristics. a Photograph and schematic cross-sectional view of the SPC-prepared In_2O_3:H TFTs. **b** HRTEM image and corresponding SAED pattern of the active layer of the TFT with In_2O_3:H channel deposited at $R[H_2] = 5\%$. **c–e** Typical transfer characteristics of the TFTs with In_2O_3 and In_2O_3:H channels deposited at various $R[H_2]$ values. Variations of **f** μ_{FE}, **g** SS, **h** V_{th}, and **i** ΔV evaluated from ten TFTs.

Table 1 Summary of the TFT properties.

R[O_2] (%)	R[H_2] (%)	μ_{FE} ($cm^2 V^{-1} s^{-1}$)	*SS* ($V dec^{-1}$)	V_{th} (V)	ΔV (V)	D_{sg} ($cm^{-2} eV^{-1}$)
1	0	-	-	-		-
1	3	142.0 (1.2)	0.41 (0.09)	0.1 (0.3)	0.2 (0.1)	1.3×10^{12}
1	5	139.2 (3.0)	0.19 (0.02)	0.2 (0.2)	0.3 (0.1)	4.7×10^{11}

The average values and standard deviations (σ) of the characteristics of ten TFTs on the same substrate. σ are shown in parentheses.

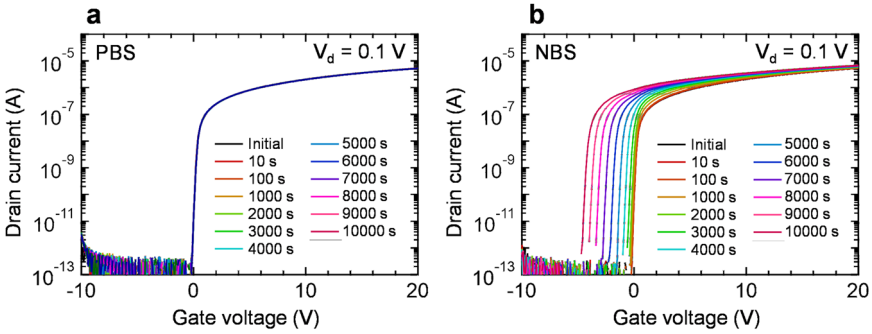

Fig. 4 Reliability of the In_2O_3:H TFT. Changes in the transfer characteristics of the In_2O_3:H ($R[H_2] = 5\%$) TFT during the **a** PBS and **b** NBS tests. The V_{gs} values under the PBS and NBS tests were +20 and −20 V, respectively.

$R[H_2] = 5\%$, which is confirmed by the optical measurements of the films shown in Fig. 2f.

The resulting transfer performance of the SPC-prepared In_2O_3:H TFT ($R[H_2] = 5\%$) was superior to that of previously reported oxide-based TFTs[38]. Although the μ_H of the In_2O_3:H ($R[H_2] = 5\%$) films decreased to 14.9 $cm^2 V^{-1} s^{-1}$ with N_e of $2.0 \times 10^{17} cm^{-3}$ by annealing at 300 °C as shown in Fig. 2c, extremely high μ_{FE} was obtained from the TFTs because a large number of carriers (10^{19}–$10^{20} cm^{-3}$) was generated at the In_2O_3:H/gate insulator interface when applying a voltage to the gate, which allows electrons to tunnel through the narrow width (<1 nm) of the grain barriers at high N_e values. The high μ_{FE} and steep *SS* of the In_2O_3:H TFTs can be attributed to the high crystallinity of In_2O_3:H, especially near the In_2O_3:H/SiO_2 gate insulator interface.

Figure 3b shows a cross-sectional conventional bright-field HRTEM image and selective area electron diffraction (SAED) pattern obtained from the SPC-prepared In_2O_3:H TFT ($R[H_2] = 5\%$). A clear lattice image was observed over the entire thickness of the In_2O_3:H channel. Moreover, there was a single crystal-like diffraction pattern in the SAED pattern, even in the thin layers, roughly at a distance of 5 nm from the SiO_2 gate insulator without detectable diffuse ring patterns, which would be attributable to an amorphous phase. This observation explains the high μ_{FE} of 139.2 $cm^2 V^{-1} s^{-1}$ in the In_2O_3:H TFTs, which is comparable to the μ_H of epitaxial single-crystal In_2O_3 films (~160 $cm^2 V^{-1} s^{-1}$)[39]. In addition, although In_2O_3:H is a polycrystalline film, the standard deviations (σ) of μ_{FE}, *SS*, V_{th}, and ΔV of the In_2O_3:H TFT ($R[H_2] = 5\%$) were 3.0 $cm^2 V^{-1} s^{-1}$, 0.02 V dec^{-1}, 0.2 V, and 0.1 V, respectively, indicating high uniformity of the TFT characteristics (shown in Fig. 3f–i and Supplementary Fig. 2).

To investigate the reliability of the SPC-prepared In_2O_3:H TFT ($R[H_2] = 5\%$), positive-bias stress (PBS) and negative-bias stress (NBS) tests were carried out under a humidity of 50%. The gate stress voltages for the PBS and NBS were +20 and −20 V, respectively. Figure 4a, b show the changes in the transfer characteristics of the In_2O_3:H TFT during the PBS and NBS tests. The In_2O_3:H TFT showed no significant positive shift in V_{th} (only +0.02 V) under the PBS test, indicating the negligible interfacial trap states in the In_2O_3:H/SiO_2 gate insulator interface as well as the high quality of the In_2O_3:H channel layer. In contrast, a large V_{th} shift of −4.4 V was observed for the NBS test, as shown in Fig. 4b. Furthermore, the V_{th} shift became more significant when the NBS test was conducted at a higher humidity of 70% (shown in Supplementary Fig. 3). Water molecules are coupled to the backchannel of the IGZO TFTs, and excess electrons are donated to the channel under NBS, resulting in a negative V_{th} shift[40,41]. Applying a passivation layer to the TFTs is effective in minimizing the influence of the atmospheric environment; however, hydrogen can diffuse into the channel through the passivation layer and increase the N_e of the channel[42]. Although the SiO_2 passive layer was applied to the SPC-grown In_2O_3:H TFT, as shown in Fig. 3a, its protection ability was insufficient because the SiO_2 film was deposited via sputtering at RT. Hence, it is believed that the reliability of In_2O_3:H TFTs can be improved by selecting the appropriate passivation layer, such as SiN, Al_2O_3, or Y_2O_3.

Discussion

In this study, we demonstrate the high-performance polycrystalline In_2O_3:H TFTs using a low-temperature SPC process. To ensure the amorphous state of the as-deposited In_2O_3:H film, a moderate amount of H_2 was introduced into the sputtering system during the In_2O_3:H deposition. The as-deposited amorphous In_2O_3:H film converted into a polycrystalline In_2O_3:H film with a grain size of around 140 nm via low-temperature SPC (at a temperature below 200 °C). As a result, a high μ_H of 104.0 $cm^2 V^{-1} s^{-1}$ was obtained for the In_2O_3:H film. This μ_H value is five times higher than that of the In_2O_3 film without H_2 introduction during sputtering. Furthermore, the N_e of the SPC-grown In_2O_3:H film decreased significantly to $2.0 \times 10^{17} cm^{-3}$ after annealing at 300 °C in ambient air; this N_e value is two orders of magnitude lower than that of the In_2O_3 film without H_2 introduction. Thus, introducing hydrogen during sputtering followed by annealing in ambient air is an effective method for improving both the crystallinity and the N_e value of In_2O_3:H films. The obtained In_2O_3:H film was employed as the channel of a TFT, and the resulting In_2O_3:H TFT exhibits an extremely high

μ_{FE} of 139.2 $cm^2V^{-1}s^{-1}$, an appropriate V_{th} of 0.2 V, and a small SS of 0.19 V dec^{-1}. HRTEM analysis of the TFT revealed the high crystallinity of cubic bixbyite near the In_2O_3:H/SiO_2 gate dielectric interface, which contributed to the high μ_{FE} of the TFT. The proposed method does not require any additional expensive equipment and/or change in the conventional oxide TFT fabrication process. Moreover, composition control of binary In_2O_3 films is easier than that of ternary and quaternary semiconductors. We believe that these SPC-grown In_2O_3:H TFTs are promising candidates for use in future transparent or flexible electronics applications.

Methods

Fabrication of In_2O_3:H TFTs. In_2O_3:H TFTs were fabricated on a heavily doped *p*-type Si substrate with a 100-nm-thick thermally grown SiO_2. The doped *p*-type Si substrate and the SiO_2 were used as the gate electrode and the gate insulator. The 30-nm-thick In_2O_3 and In_2O_3:H channels were deposited via pulsed direct-current (DC) magnetron sputtering without substrate heating from a ceramic In_2O_3 target using a mixture of Ar, O_2, and H_2 gases. The O_2 and H_2 gas flow ratios are $R[O_2] = O_2/(Ar + O_2 + H_2)$ and $R[H_2] = H_2/(Ar + O_2 + H_2)$, respectively. For the $Ar + O_2$-sputtered In_2O_3 film, $R[O_2]$ was set to 1% without H_2 introduction. For the $Ar + O_2 + H_2$-sputtered In_2O_3 film (In_2O_3:H), $R[H_2]$ varied from 3 to 5%, whereas $R[O_2]$ was fixed at 1%. The deposition pressure and DC power were maintained at 0.6 Pa and 50 W, respectively. The base pressure before gas introduction was below 6×10^{-5} Pa. The In_2O_3 and In_2O_3:H films were then annealed in ambient air at 300 °C for 1 h. After annealing, a 100-nm-thick SiO_2 film was deposited via reactive sputtering without substrate heating. This film served as a passive layer. Subsequently, Al source/drain electrodes were deposited via sputtering. Finally, In_2O_3 and In_2O_3:H TFTs were annealed at 250 °C in ambient air for 1 h. The In_2O_3, SiO_2, and Al films were deposited through a shadow mask. Both the channel length and the width were 300 μm.

Characterization of the In_2O_3:H films and TFTs. Structural, electrical, and optical measurements were conducted on the 50-nm-thick In_2O_3 and In_2O_3:H films deposited on a synthetic quartz substrate. The films' structural changes were evaluated through X-ray diffraction (XRD) (Philips corp., X'pert) with CuKα radiation and electron backscattering diffraction (EBSD) (EDAX-TSL Hikari High Speed EBSD Detector). The films' carrier concentrations (N_e) and Hall mobility (μ_H) were determined via Hall effect measurements (Accent, HL5500PC) using the van der Pauw geometry at room temperature (RT). The films' optical properties were measured via spectrophotometry (Hitachi, U-4100). The current–voltage characteristics were measured using a semiconductor parameter analyzer (Keysight, E5270B) at RT in the dark. High-resolution transmission electron microscopy (HRTEM) (JEOL, JSM-7001F) analysis was also conducted to observe the microstructure of the In_2O_3:H channel in the TFTs.

Data availability

The authors declare that the all the data supporting the finding of this study are available within this article and its Supplementary Information files and are available from the corresponding author on reasonable request.

Received: 31 August 2021; Accepted: 11 January 2022;
Published online: 28 February 2022

References

1. Hirao, T. et al. Novel top-gate zinc oxide thin-film transistors (ZnO TFTs) for AMLCDs. *J. Soc. Inf. Disp.* **15**, 17 (2007).
2. Park, S.-H. K. et al. 4.3: Transparent ZnO thin film transistor array for the application of transparent AM-OLED display. *SID Symp. Dig. Tech. Pap.* **37**, 25 (2006).
3. Inoue, H. et al. Nonvolatile memory with extremely low-leakage indium-gallium-zinc-oxide thin-film transistor. *IEEE J. Solid State Circuits* **47**, 2258–2265 (2012).
4. Huang, X. et al. Large-swing a-IGZO inverter with a depletion load induced by laser annealing. *IEEE Electron Device Lett.* **35**, 1034–1036 (2014).
5. Furuta, M. et al. Photocurrent and persistent photoconductivity in zinc oxide thin-film transistors under ultraviolet-light irradiation. *Jpn J. Appl. Phys.* **50**, 110204 (2011).
6. Kaczmarski, J., Jankowska-Śliwińska, J. & Borysiewicz, M. IGZO MESFET with enzyme-modified Schottky gate electrode for glucose sensing. *Jpn J. Appl. Phys.* **58**, 090603 (2019).
7. Magari, Y. et al. Record-high-performance hydrogenated In-Ga-Zn-O flexible Schottky diodes. *ACS Appl. Mater. Interfaces* **12**, 47739–47742 (2020).
8. Magari, Y. et al. Low-temperature (150 °C) processed metal-semiconductor field-effect transistor with a hydrogenated In-Ga-Zn-O stacked channel. *Jpn J. Appl. Phys.* **59**, 2–7 (2020).
9. Nomura, K. et al. Room-temperature fabrication of transparent flexible thin-film transistors using amorphous oxide semiconductors. *Nature* **432**, 488–492 (2004).
10. Kamiya, T. & Hosono, H. Material characteristics and applications of transparent amorphous oxide semiconductors. *NPG Asia Mater.* **2**, 15–22 (2010).
11. Ohshima, H. Value of LTPS: present and future. *SID Int. Symp. Dig. Tech. Pap.* **45**, 75–78 (2014).
12. Aikawa, S., Nabatame, T. & Tsukagoshi, K. Effects of dopants in InOx-based amorphous oxide semiconductors for thin-film transistor applications. *Appl. Phys. Lett.* **103**, 1–5 (2013).
13. Nakata, M., Zhao, C. & Kanicki, J. DC sputtered amorphous In–Sn–Zn–O thin-film transistors: electrical properties and stability. *Solid State Electron.* **116**, 22–29 (2016).
14. Taniguchi, S., Yokozeki, M., Ikeda, M. & Suzuki, T. K. Transparent oxide thin-film transistors using n-$(In_2O_3)_{0.9}(SnO_2)_{0.1}$/$InGaZnO_4$ modulation-doped heterostructures. *Jpn J. Appl. Phys.* **50**, 2–6 (2011).
15. Furuta, M. et al. Heterojunction channel engineering to enhance performance and reliability of amorphous In–Ga–Zn–O thin-film transistors. *Jpn J. Appl. Phys.* **58**, 090604 (2019).
16. Li, X., Geng, D., Mativenga, M. & Jang, J. High-speed dual-gate a-IGZO TFT-based circuits with top-gate offset structure. *IEEE Electron Device Lett.* **35**, 461–463 (2014).
17. Park, E. J. et al. Transparent flexible high mobility TFTs based on ZnON semiconductor with dual gate structure. *IEEE Electron Device Lett.* **41**, 401–404 (2020).
18. Zan, H. W. et al. Dual gate indium-gallium-zinc-oxide thin film transistor with an unisolated floating metal gate for threshold voltage modulation and mobility enhancement. *Appl. Phys. Lett.* **98**, 153506 (2011).
19. Lee, B. H., Sohn, A., Kim, S. & Lee, S. Y. Mechanism of carrier controllability with metal capping layer on amorphous oxide SiZnSnO semiconductor. *Sci. Rep.* **9**, 1–7 (2019).
20. Jeong, H. J. et al. Ultra-high-speed intense pulsed-light irradiation technique for high-performance zinc oxynitride thin-film transistors. *ACS Appl. Mater. Interfaces* **11**, 4152–4158 (2019).
21. Nam, Y. et al. Effect of RTP annealing using UV and DUV light on the properties of the Al-IZTO TFTs. *SID Int. Symp. Dig. Tech. Pap.* **49**, 1249–1251 (2018).
22. Nomura, K. et al. Thin-film transistor fabricated in single-crystalline transparent oxide semiconductor. *Science* **300**, 1269–1272 (2003).
23. Lany, S. et al. Surface origin of high conductivities in undoped In_2O_3 thin films. *Phys. Rev. Lett.* **108**, 2–6 (2012).
24. Koida, T., Ueno, Y. & Shibata, H. In_2O_3-based transparent conducting oxide films with high electron mobility fabricated at low process temperatures. *Phys. Status Solidi* **215**, 1–14 (2018).
25. Dhananjay & Chu, C. W. Realization of In_2O_3 thin film transistors through reactive evaporation process. *Appl. Phys. Lett.* **91**, 1–4 (2007).
26. Si, M. et al. Why In_2O_3 can make 0.7 nm atomic layer thin transistors. *Nano Lett.* **21**, 500–506 (2021).
27. Koretomo, D., Hashimoto, Y., Hamada, S., Miyanaga, M. & Furuta, M. Influence of a SiO_2 passivation on electrical properties and reliability of In-W-Zn-O thin-film transistor. *Jpn J. Appl. Phys.* **58**, 018003 (2019).
28. Yang, J. H. et al. Highly stable AlInZnSnO and InZnO double-layer oxide thin-film transistors with mobility over 50 cm^2/V·s for high-speed operation. *IEEE Electron Device Lett.* **39**, 508–511 (2018).
29. Choi, I. M. et al. Achieving high mobility and excellent stability in amorphous In-Ga-Zn-Sn-O thin-film transistors. *IEEE Trans. Electron Devices* **67**, 1014–1020 (2020).
30. Kamiya, T., Nomura, K. & Hosono, H. Electronic structures above mobility edges in crystalline and amorphous In-Ga-Zn-O: percolation conduction examined by analytical model. *IEEE/OSA J. Disp. Technol.* **5**, 462–467 (2009).
31. Yang, H. J. et al. High-performance thin-film transistors with an atomic-layer-deposited indium gallium oxide channel: a cation combinatorial approach. *ACS Appl. Mater. Interfaces* **12**, 52937–52951 (2020).
32. Furuta, M. et al. High mobility hydrogenated polycrystalline In–Ga–O (IGO:H) thin-film transistors formed by Solid phase crystallization. *SID Symp. Dig. Tech. Pap.* **52**, 69 (2021).
33. Koida, T. Amorphous and crystalline In_2O_3-based transparent conducting films for photovoltaics. *Phys. Status Solidi* **214**, 1600464 (2017).
34. Nomura, K., Kamiya, T., Ohta, H., Hirano, M. & Hosono, H. Defect passivation and homogenization of amorphous oxide thin-film transistor by wet O_2 annealing. *Appl. Phys. Lett.* **93**, 1–4 (2008).

35. King, P. D. C. et al. Shallow donor state of hydrogen in In_2O_3 and SnO_2: implications for conductivity in transparent conducting oxides. *Phys. Rev. B* **80**, 1–4 (2009).
36. Preissler, N., Bierwagen, O., Ramu, A. T. & Speck, J. S. Electrical transport, electrothermal transport, and effective electron mass in single-crystalline In_2O_3 films. *Phys. Rev. B* **88**, 1–10 (2013).
37. Ellmer, K. & Vollweiler, G. Electrical transport parameters of heavily-doped zinc oxide and zinc magnesium oxide single and multilayer films heteroepitaxially grown on oxide single crystals. *Thin Solid Films* **496**, 104–111 (2006).
38. Lee, S. Y. Comprehensive review on amorphous oxide semiconductor thin film transistor. *Trans. Electr. Electron Mater.* **21**, 235–248 (2020).
39. Weiher, R. L. Electrical properties of single crystals of indium oxide. *J. Appl. Phys.* **33**, 2834–2839 (1962).
40. Park, J. S., Jeong, J. K., Chung, H. J., Mo, Y. G. & Kim, H. D. Electronic transport properties of amorphous indium-gallium-zinc oxide semiconductor upon exposure to water. *Appl. Phys. Lett.* **92**, 90–93 (2008).
41. Yang, J. et al. H_2O adsorption on amorphous In-Ga-Zn-O thin-film transistors under negative bias stress. *Appl. Phys. Lett.* **111**, 073506 (2017).
42. Chen, H. C. et al. Investigation of the capacitance–voltage electrical characteristics of thin-film transistors caused by hydrogen diffusion under negative bias stress in a moist environment. *ACS Appl. Mater. Interfaces* **11**, 40196–40203 (2019).

Acknowledgements

This work was partly supported by JSPS KAKENHI Grant No. 20K22415 and Iketani Science and Technology Foundation No.0331062-A. The EBSD experiment was supported by Next Generation Tatara Co-Creation Centre, Shimane University.

Author contributions

M.F. conceived the concept and supported the device analysis. Y.M. designed the research and experiments. Y.M. performed the film deposition, device fabrication, and their analysis. T.K. supported the electrical and optical measurements. W.Y. designed and fabricated pulse-DC sputtering apparatus for film deposition and set up experimental environment for TFT fabrication and evaluation, and supported EBSD measurements. All authors contributed to the discussions and commented on the manuscript.

Competing interests

The authors declare no competing interests.

Additional information

Supplementary information The online version contains supplementary material available at https://doi.org/10.1038/s41467-022-28480-9.

Correspondence and requests for materials should be addressed to Yusaku Magari.

Peer review information *Nature Communications* thanks Mamatimin Abbas, M. C. Santhosh Kumar and the other, anonymous, reviewer for their contribution to the peer review of this work.